

The distance of quasar outflows from the central source: The first consistent values from emission and absorption determinations.

MAYANK SHARMA,¹ NAHUM ARAV,¹ QINYUAN ZHAO,^{2,3,4} MARYAM DEGHANIAN,¹ DOYEE BYUN,¹ GWEN WALKER,¹ LUMING SUN,⁵ LU SHEN,^{6,7}
YULONG GAO,^{8,9} GUILIN LIU,^{2,3} AND JUNFENG WANG⁴

¹Department of Physics, Virginia Tech, Blacksburg, VA 24061, USA

²CAS Key Laboratory for Research in Galaxies and Cosmology, Department of Astronomy, University of Science and Technology of China, Hefei 230026, China

³School of Astronomy and Space Sciences, University of Science and Technology of China, Hefei 230026, China

⁴Department of Astronomy, Xiamen University, Xiamen, Fujian 361005, China

⁵Department of Physics, Anhui Normal University, Wuhu, Anhui 241002, China

⁶Department of Physics and Astronomy, Texas A&M University, College Station, TX, 77843-4242 USA

⁷George P. and Cynthia Woods Mitchell Institute for Fundamental Physics and Astronomy, Texas A&M University, College Station, TX, 10 77843-4242 USA

⁸School of Astronomy and Space Science, Nanjing University, Nanjing 210093, PR China

⁹Key Laboratory of Modern Astronomy and Astrophysics (Nanjing University), Ministry of Education, Nanjing 210093, PR China

ABSTRACT

Measuring the distance of quasar outflows from the central source (R) is essential for determining their importance for AGN feedback. There are two methods to measure R : 1) A direct determination using spatially resolved Integral Field Spectroscopy (IFS) of the outflow in emission. 2) An indirect method which uses the absorption troughs from ionic excited states. The column density ratio between the excited and resonance states yields the outflow number density. Combined with a knowledge of the outflow's ionization parameter, R can be determined. Generally, the IFS method probes R range of several kpc or more, while the absorption method usually yields R values of less than 1kpc. There is no inconsistency between the two methods as the determinations come from different objects. Here we report the results of applying both methods to the same quasar outflow, where we derive consistent determinations of $R \approx 5$ kpc. This is the first time where the indirect absorption R determination is verified by a direct spatially resolved IFS observation. In addition, the velocities (and energetics) from the IFS and absorption data are also found to be consistent. Therefore, these are two manifestations of the same outflow. In this paper we concentrate on the absorption R determination for the outflow seen in quasar 3C 191 using VLT/X-shooter observations. We also reanalyze an older absorption determination for the outflow based on Keck/HIRES data and find that revised measurement to be consistent with ours. Our companion paper details the IFS analysis of the same object.

Keywords: Galaxies (573), Active galactic nuclei (16), Quasars (1319), AGN host galaxies (2017), Quasar absorption line spectroscopy (1317)

1. INTRODUCTION

Active galactic nuclei (AGN) feedback serves as an important link in the co-evolution of supermassive black holes (SMBHs) and their host galaxies. It has thus become an essential feature of modern theories of galaxy formation (e.g., Cattaneo et al. 2009; Silk & Mamon 2012; Hlavacek-Larrondo et al. 2024) and state-of-the-art cosmological simulations (e.g., Dubois et al. 2012; Davé et al. 2019; Donnari et al. 2021). In the quasar mode of AGN feedback, power-

ful outflows are driven by SMBHs accreting close to the Eddington limit. The energy and momentum carried by these outflows can be re-deposited in the surrounding medium and thus contribute to various feedback processes. To assess this contribution quantitatively, it is important to determine the spatial extent of the outflowing gas (R), its mass (M), mass flow rate (\dot{M}) and kinetic luminosity (\dot{E}_k) from observations.

Observational signatures of quasar outflows are detected primarily: (a) in emission, as spatially-resolved galactic scale winds studied using Integral Field Spectroscopy (IFS) (and other techniques such as long-slit spectroscopy) and (b) in absorption, as blueshifted troughs in the quasar spectrum observed as a result of the intersection of our line of sight with

the outflowing gas. Both these analysis techniques have been utilized greatly over the last two decades for their distinct advantages. The absorption analysis is much richer in spectroscopic information and has thus allowed the study of a wide range of physical parameters (e.g., density and ionization state) in the outflows. The detection of absorption troughs from metastable excited states plays a crucial role in the analysis as their population ratio with the resonance state is a reliable indicator of the outflow's number density. The ionization state is typically determined through a detailed photoionization modeling of the outflow, and combined with the number density leads (using eqn. 4) to an indirect determination for the distance of the outflow from the central source (e.g., Hamann et al. 2001; de Kool et al. 2001; Moe et al. 2009; Bautista et al. 2010; Dunn et al. 2010; Aoki et al. 2011; Borguet et al. 2012a,b; Arav et al. 2013; Lucy et al. 2014; Finn et al. 2014; Chamberlain & Arav 2015; Chamberlain et al. 2015; Miller et al. 2018, 2020; Xu et al. 2018, 2020, 2021; He et al. 2022; Byun et al. 2022a,b, 2024a,b; Walker et al. 2022; Dehghanian et al. 2024). While these studies have revealed a wide range for the distance by placing the outflows at a few pc to several kpc, most of them are still found to be at distances less than a few kpc (Arav et al. 2018; Xu et al. 2019).

IFS analysis on the other hand directly measures the spatial extent of large-scale outflows and provides valuable insights into their morphology and kinematic structure. Recent IFS studies have highlighted the prevalence of kpc scale outflows in AGNs (e.g., Nesvadba et al. 2008; Alexander et al. 2010; Rupke & Veilleux 2011, 2013; Harrison et al. 2012, 2014; Liu et al. 2013, 2014, 2015; Karouzos et al. 2016; Kakkad et al. 2020; Wylezalek et al. 2020; Kim et al. 2023; Shen et al. 2023; Travascio et al. 2024; Parlanti et al. 2024; Übler et al. 2024). Emission line diagnostics also exist for determining the electron number density of these outflows (Holt et al. 2011; Baron & Netzer 2019), however they are subject to larger uncertainties as inconsistencies have been revealed between different commonly used methods (Davies et al. 2020).

Although these two methods of distance determinations have led to different scales for the outflows, they are not inconsistent with each other. This is because these methods have either been applied to different objects, or to different outflow phases for the same object (e.g., Noterdaeme et al. 2021; Zhao & Wang 2023; Bischetti et al. 2024). However, attempts to verify the indirect distance determination from absorption analysis through IFS mapping have also only seen limited success (Liu et al. 2015, also see section 5.2 for a detailed discussion), thus highlighting the missing link between these two analysis techniques. In this paper (and the companion paper by Zhao et al. 2025, in press.), we present the first consistent distance determination for a quasar outflow from

the two analysis techniques, in the form of an ionized outflow in quasar 3C 191. This paper details the absorption analysis for the outflow while its IFS analysis is detailed in Zhao et al. (2025, in press.).

3C 191 (J2000: RA=08:04:47.97; DEC: +10:15:23.70) is a radio-loud quasar with a bipolar radio structure spanning ~ 5 arcsec (~ 42 kpc at the quasar redshift) (Pearson et al. 1985; Akujor et al. 1994). It was one of the first quasars to show an extensive absorption system in its spectrum as identified by Burbidge et al. 1966 and Stockton & Lynds 1966. The detection of Si II ground and excited states with high dispersion observations allowed an estimation for the electron number density with $n_e \sim 10^3 \text{ cm}^{-3}$ and the distance of the outflow component from the central source was determined to be $R \sim 10$ kpc (Bahcall et al. 1967; Williams et al. 1975). However, Hamann et al. 2001 analyzed a high-resolution spectrum of 3C 191 and obtained $n_e \sim 300 \text{ cm}^{-3}$ and $R \sim 28$ kpc for the outflow component. Thus, while there is a slight disagreement between these analysis for the physical parameters (also addressed in section 4.6 of Hamann et al. 2001), they nonetheless suggest a galactic scale absorption line outflow. This makes the outflow in 3C 191 a great choice for a complementary analysis using both absorption and IFS techniques.

In this paper, we present a study of the X-shooter (Ver-net et al. 2011) spectrum of the quasar 3C 191 obtained on the Very Large Telescope (VLT). Section 2.1 describes the observation and how the redshift and normalized spectrum were obtained for our analysis. In Section 2.2, we analyse the spectrum to extract the column densities of the observed troughs, which allows us to obtain a photoionization model for the outflow and its electron number density. In section 2.3, we determine the distance of the outflow from the central source and its energetics. In section 3, we revisit the analysis of Hamann et al. (2001), and update the outflow parameters obtained by them from the Keck/HIRES spectrum. Section 4 compares the results of our absorption analysis of the outflow with the IFS analysis of Zhao et al. (2025, in press.). We discuss important aspects of our results in section 5 and conclude the paper with a summary in section 6. Throughout the paper, we adopt a standard Λ CDM cosmology with $h = 0.677$, $\Omega_m = 0.310$ and $\Omega_\Lambda = 0.690$ (Planck Collaboration et al. 2020).

2. VLT X-SHOOTER ANALYSIS

2.1. Data Overview

2.1.1. Observation and Data Acquisition

3C 191 was observed with VLT/X-shooter on 03 December, 2013, with a total exposure time of 3000 secs (as part of program 092.B-0393, PI: Leipski). The data covers a spectral range of 2989-10200 Å, with resolution $R \approx 4100$. The spectrum was processed by ESO through their standard pipelines

(see Modigliani et al. 2010, for a detailed description of the X-shooter pipeline) to remove instrument and atmospheric signatures and perform flux and wavelength calibration. The processed spectrum was then made available on the ESO Science archive¹. Several noise spikes less than 3 pixels wide (originating from impact of cosmic rays with the detector) were seen throughout the processed spectrum. We omitted these affected pixels using three sigma clipping and obtained the finalized spectrum (shown in Fig. 1) for our analysis.

2.1.2. Redshift Determination

Zhao et al. (2025, in press.) determined the redshift of 3C 191 using the narrowest component of the [O III] 5007 Å emission line extracted from the central 0.25'' around the quasar nucleus. They determined the systematic redshift of the quasar to be $z = 1.9527 \pm 0.0003$ (see their section 3.1 for a detailed description of the emission model). This was also found to be in agreement with the redshift determined from [O II] $\lambda\lambda$ 3727, 3729 doublet ($z = 1.9527 \pm 0.0003$) detected in emission in the VLT/X-shooter spectrum and therefore we adopt this redshift for our analysis.

2.1.3. Unabsorbed Emission Modeling

In order to identify the troughs and determine their column densities, we need to obtain a normalized spectrum by dividing the data by the unabsorbed emission model. In the spectrum of 3C 191, we first select spectral regions free from significant emission or absorption ($\lambda_{obs} \approx 3165, 3370, 4000, 4300$ and 5300 Å) to use as anchor points for our continuum fit. We find that a single power law is unable to describe the emission in the observed wavelength range analysed in this paper and therefore we employ a broken power law of the form $F_\lambda = F_{4000}(\lambda_{obs}/4000)^\alpha$, where α takes different values before (α_1) and after (α_2) $\lambda_{obs} = 4000$ Å. The best fit parameters for the model obtained using non-linear least squares are: $\alpha_1 = 0.34 \pm 0.09$, $\alpha_2 = -1.08 \pm 0.01$ and $F_{4000} = 1.104 (\pm 0.003) \times 10^{-16}$ ergs s⁻¹ cm⁻² Å⁻¹ with χ_{red}^2 (reduced chi-square) = 0.754.

The X-Shooter spectrum also shows clear signature of many prominent emission features and thus we obtain a best-fit model using non-linear least squares for each of these features by considering absorption free regions in their vicinity. The Ly α /N v complex is modeled with four independent Gaussian components. The C IV emission feature also requires separate broad emission line (BEL) and narrow emission line (NEL) components and was therefore modeled using two independent Gaussians. The Si IV emission feature on the other hand, is well modeled with a single Gaussian component. Finally, we also detect weak emission in two regions: $3800 \text{ \AA} \lesssim \lambda_{obs} \lesssim 3900 \text{ \AA}$ and $4700 \text{ \AA} \lesssim \lambda_{obs} \lesssim 5000 \text{ \AA}$. Based

Table 1. Wavelength ranges used for fitting the emission lines in the VLT/X-Shooter spectrum and the resulting χ_{red}^2 .

Complex	Lines	Wavelength Range (Å)	χ_{red}^2
1	Ly α + N v	3480-3485, 3493-3498	1.261
		3533-3543, 3562-3565	
		3595-3636, 3667-3700	
		3740-3770	
2	O I + Si II	3795-3835, 3870-3905	0.656
3	Si IV	4075-4090, 4117-4123	0.691
		4140-4146, 4180-4200	
4	C IV	4400-4480, 4530-4540	0.944
		4580-4630	
5	He II + O III] + Al II + Fe II	4672-4732, 4745-4880	0.999
		4900-4910, 4931-4990	

on the composite quasar SDSS spectra of Berk et al. (2001), the first region is likely to be a blend of O I/Si II, whereas the latter could contain contribution from He II along with a blend of O III]/Al II/Fe II. We are able to model these regions with one and three independent Gaussians respectively. Table. 1 reports the wavelength ranges (rounded off to the nearest integer) used as anchor for fitting each emission complex and the χ_{red}^2 for the respective fits. Combining the continuum model and the different emission components gives us the unabsorbed emission model, which is shown in Fig. 1 by the red dashed curve.

2.2. Spectral Analysis

2.2.1. Identifying Outflow Systems

Having determined the systematic redshift and modeled the unabsorbed emission, we identify the main absorption system for the low ionization species (Si II, C II, Al II, AL III and Si III), spanning a velocity range $-950 \lesssim v \lesssim -500$ km s⁻¹, with the deepest absorption at $v \sim -720$ km s⁻¹. The same system is detected in the high ionization species (C IV, Si IV, S IV and N v) as well. However, the high ionization troughs are broader and show a shift in velocity space with the deepest absorption at $v \sim -800$ km s⁻¹. Similar shift in velocities for higher ionization potential ions has been previously reported in absorption troughs from an outflow in PKS J0352-0711 by Miller et al. (2020). Based on the width of the C IV trough ($\Delta v \sim 1500$ km s⁻¹), the outflow system is characterized as a mini broad absorption line (mini-BAL; Hamann & Sabra 2004).

2.2.2. Column Density Determination

The ionic column densities N_{ion} of the various observed species can be obtained from the troughs by assuming an absorber model for the cloud. The simplest model, known as

¹ <https://archive.eso.org/scienceportal>

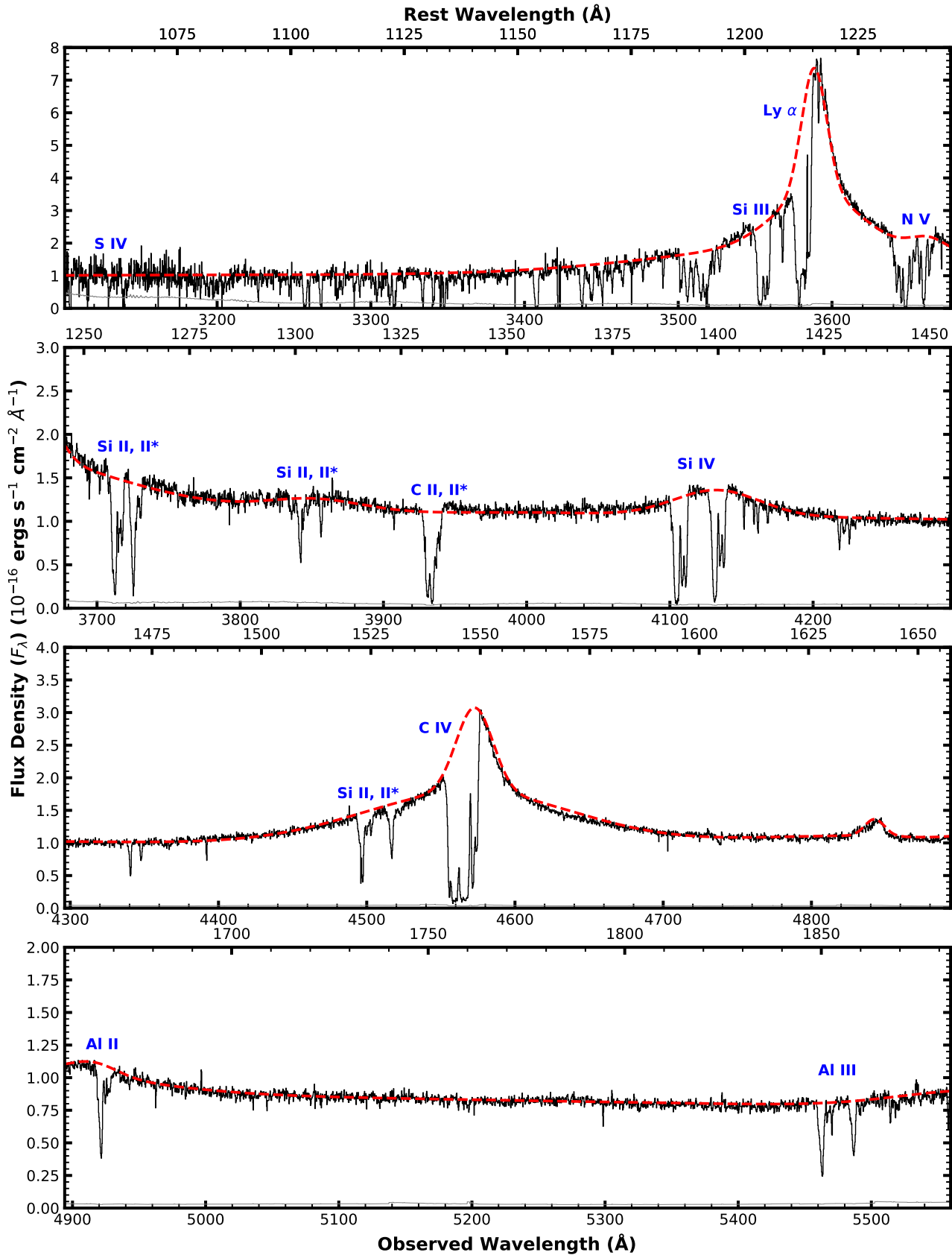


Figure 1. VLT/X-shooter spectrum of 3C 191. The red dashed curve shows our modeled continuum along with the emission features. Important absorption features from the identified outflow system are marked in blue. The noise in the VLT/X-shooter flux is shown in gray.

the apparent optical depth (AOD) model assumes a homogeneous outflow that completely covers the source. In this case, the normalized intensity profile as a function of velocity $I(v)$ is related to the optical depth $\tau(v)$ as $I(v) = e^{-\tau(v)}$. N_{ion} for a transition with rest wavelength λ (in Angstroms) and oscillator strength f is then given as (Savage & Sembach 1991):

$$N_{ion} = \frac{m_e c}{\pi e^2 f \lambda} \int \tau(v) dv = \frac{3.8 \times 10^{14}}{f \lambda} \int \tau(v) dv \quad [\text{cm}^{-2}] \quad (1)$$

where m_e is electron mass, c is the speed of light, e is elementary charge. The homogeneous AOD model does not account for partial line of sight covering of the outflow and line saturation and therefore can only lead to lower limits for N_{ion} in most cases. If troughs from two or more lines corresponding to the same lower energy level of an ion are observed, we can employ a partial covering (PC) model. In this two-parameter model, the absorber is assumed to be covering a (velocity dependent) fraction $C(v)$ of a constant emission source. The normalized intensity for the two lines are then given as:

$$\begin{aligned} I_1(v) &= 1 - C(v) + C(v) \cdot e^{-\tau(v)} \\ I_2(v) &= 1 - C(v) + C(v) \cdot e^{-R\tau(v)} \end{aligned} \quad (2)$$

where R is the expected line strength ratio given by $R = (g_i f_{ik} \lambda)_2 / (g_i f_{ik} \lambda)_1$ (where g_i is the degeneracy of the lower level i , f_{ik} is the oscillator strength of the transition between levels i and k , and λ is the transition's wavelength). Having obtained $I_1(v)$ and $I_2(v)$ from the spectrum, $C(v)$ and $\tau(v)$ can be obtained numerically by solving for eqns. (2) simultaneously (see Arav et al. 1999, 2005, for a detailed description of the model).

We model the troughs in velocity space using a Gaussian profile for the optical depth and note that for most of the observed ionic species (H I, N v, C II, C IV, Si III and Si IV), the troughs appear saturated and therefore only lower limits for N_{ion} can be obtained for them based on the AOD model. We detect troughs from two different ionized species of Al: Al III $\lambda\lambda$ 1855, 1863 and Al II 1671 Å. We first model the Al III 1863 Å trough with a Gaussian profile and then use this model as a template for the Al III 1855 Å and Al II 1671 Å troughs by fixing the centroid and width of the profile while allowing its depth to vary independently (see Appendix A for an alternate multi-component modeling and the difference between the two approaches). The best-fit models (shown in Fig. 2) are determined by non-linear least squares. We note that for Al II, the deepest part of the model and the trough show a slight offset ($\sim 30 \text{ km s}^{-1}$). However, as this shift is less than one resolution element in the velocity space ($\sim 73 \text{ km s}^{-1}$), we continue to use this model for our analysis as it is physically motivated. As the two Al III lines originate from the same lower energy level, we can use the partial covering method to obtain a measurement for its N_{ion} . We find

that the N_{ion} determined using the PC method differs by less than 20 % from the AOD determination, thus indicating that these troughs are not affected greatly by non-black saturation. As the Al II 1671 Å trough appears shallower than the Al III 1855 Å trough, it would be affected even less by non-black saturation (see section 2.2 in Arav et al. 2018, for a detailed description of non-black saturation). This allows us to use the N_{ion} determined from the AOD method as a measurement. Reliable measurements of column densities from two different ionization states of Al plays an important role in our photoionization analysis, which we describe in detail in the next section.

For Si II, we detect multiple troughs originating from both the ground state and the 287 cm^{-1} metastable excited state. Among the detected Si II transitions, the 1304 Å line has the smallest oscillator strength. It also appears much shallower than the other deeper Si II troughs (at 1260 and 1527 Å) and can thus be considered unsaturated. Using the same argument to compare the different Si II* transitions at 1265, 1309 and 1533 Å shows the 1309 Å trough can also be considered as unsaturated. Therefore, the AOD column densities derived from the Si II/II* 1304/1309 Å transitions can be used as measurements. Our modeling of these troughs follows the same procedure as that of the Al troughs. We first model the Si II* 1309 Å trough with a Gaussian profile and use this as the template for obtaining the best-fit model for the Si II 1304 Å trough (shown in Fig. 3).

We summarize the determined column density measurements and limits for the detected troughs in Table. 2, along with the predictions of our best-fit photoionization model (section 2.2.3). The reported errors include the uncertainty in determining the best-fit model for the unabsorbed emission. We first obtain the $1-\sigma$ errors for the different components of our best-fit emission model (shown in red in Fig. 1). Using them we construct two additional continuum models in which each component is shifted by $+\sigma$ and $-\sigma$, respectively. We use these new continuum levels to re-normalize the VLT/X-Shooter spectrum individually and obtain the column densities of the different ionic species for them. Their deviation from the column densities obtained for the best-fit emission model (reported in Table. 2) allows us to estimate their uncertainty due to our modeling of the emission features. We add them in quadrature with the $1-\sigma$ uncertainties obtained similarly for our modeling of the absorption troughs. For Al II, Al III and Si II, we also include the uncertainty due to our choice of models for their troughs as outlined in Table. 4 (see Appendix A for a comparison between the single component and multi-component approach).

2.2.3. Photoionization modeling

Ionized outflows are dominated by photoionization equilibrium (Davidson & Netzer 1979; Krolik 1999; Osterbrock

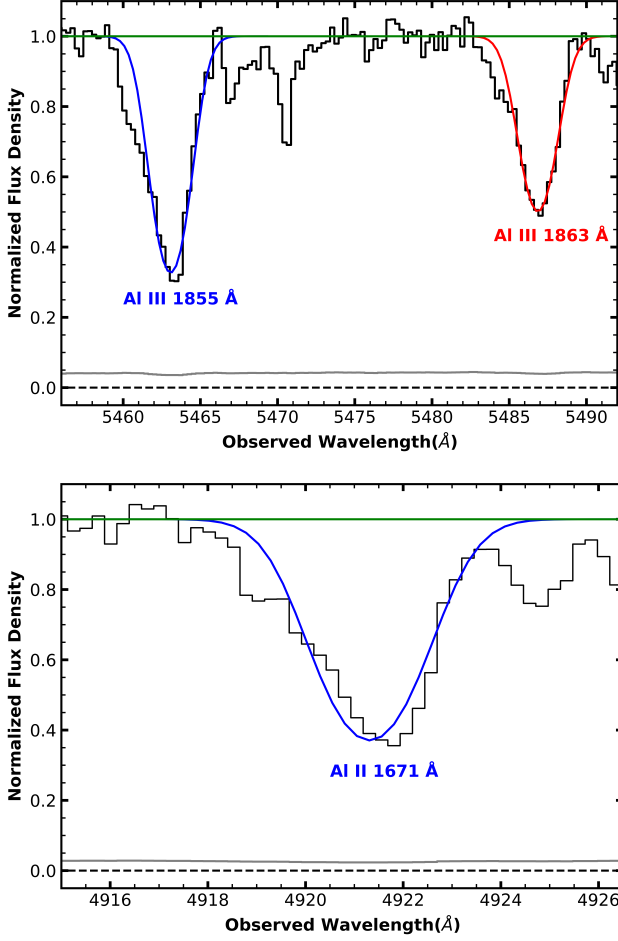


Figure 2. Detected troughs for the Al III 1855 and 1863 Å (top) and Al II 1671 Å (bottom) transitions along with their Gaussian models. The Gaussian models are based on the Al III 1863 Å trough, and then its template with fixed centroid and width is scaled to match the depth of the Al III 1855 Å and the Al II 1671 Å trough. The solid green lines represents the local continuum model. The gray line shows the noise in the VLT/X-shooter flux.

& Ferland 2006, and references therein) and are thus characterized by their total hydrogen column density (N_H) and ionization parameter (U_H), which is related to the rate of ionizing photons emitted by the source (Q_H) by:

$$U_H = \frac{Q_H}{4\pi R^2 n_H c} \quad (3)$$

where R is the distance between the central emission source and the observed outflow component, c is the speed of light, and n_H is the hydrogen number density. Q_H is determined by: (a) the choice of the spectral emission distribution (SED) that is incident upon the outflow, (b) the observed flux of the object's continuum at a specified wavelength, (c) the redshift of the object and (d) the choice of cosmology. Having determined the column densities of the observed ionic species, we can constrain the physical state of the gas, using the spec-

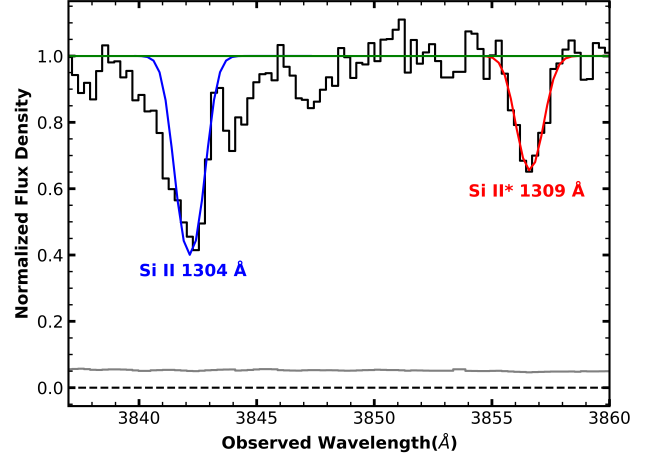


Figure 3. Observed troughs for the Si II 1304 Å and Si II* 1309 Å transitions along with their Gaussian models. The model is based on the Si II* excited trough, and then its template with fixed centroid and width is scaled to match the depth of the Si II trough. The solid green line represents the local continuum model. The gray line shows the noise in the VLT/X-shooter flux.

Table 2. Ionic column densities for the outflow in 3C 191.

Ion	$\log(N_{ion})^a$ [cm^{-2}]	$\log(N_{mod})^b$ [cm^{-2}]
H I	$> 14.93_{-0.10}$	17.28
C II	$> 14.90_{-0.09}$	15.21
C II*	$> 15.07_{-0.08}$	-
C IV	$> 15.53_{-0.10}$	16.30
N V	$> 15.31_{-0.08}$	14.63
Al II	$13.29^{+0.06}_{-0.07}$	13.29
Al III	$13.96^{+0.07}_{-0.09}$	13.96
Si II	$14.48^{+0.04}_{-0.04}$	14.25
Si II*	$14.21^{+0.05}_{-0.07}$	-
Si III	$> 14.26_{-0.08}$	15.46
Si IV	$> 14.81_{-0.07}$	15.56
S IV	$14.89^{+0.08}_{-0.10}$	15.29
S IV*	$< 13.89^{+0.09}$	-

NOTE—(a) Measured column densities for the outflow from the VLT/X-shooter spectrum. (b) Ionic column densities predicted by the best-fit CLOUDY model shown by the black dot in Fig. 4. The model values for C II, Si II and S IV include the contribution from their excited states.

tral synthesis code CLOUDY (vers. C23.01 Chatzikos et al. 2023) which solves the equations of photoionization equilibrium in the outflow. The outflow is modeled as a plane parallel slab with a constant n_H and solar abundance, and is irradiated upon by the modeled SED from the quasar HE0238-1904 (Arav et al. 2013), which is the best empirically determined SED in the extreme UV where most of the ionizing photons come from. Fig. 4 shows the result of our photoionization modeling. Using the methodology described by Edmonds et al. (2011), N_H and U_H are varied in steps of 0.1 dex, keeping all other parameters (n_H , abundances and the incident SED) constant, leading to a two dimensional grid of models in the parameter space with predictions for all the N_{ions} in the slab. The different colored contours represent the allowed values in the (N_H, U_H) phase space which correspond to the observed column density constraints for the ionic species. The strongest such constraint comes from the column density measurements of the two Al ions. The ratio of the column densities of Al II and Al III serves as an indicator of the ionization state of the outflow which is independent of the assumed abundances. Therefore based only on the Al II and Al III N_{ion} measurements, we obtain $\log N_H = 20.50^{+0.13}_{-0.16}$ [cm^{-2}] and $\log U_H = -2.06^{+0.12}_{-0.14}$. This solution is shown in Fig. 4, surrounded by an error ellipse that contains the phase space values within one standard deviation of our best-fit solution. We use this solution for the rest of our analysis. As can be seen, this solution underpredicts the Si II column density (traced by the blue curve). Furthermore, the constraint for Si II is almost parallel to that of Al II and therefore they cannot both simultaneously be satisfied by any point in the (N_H, U_H) parameter space. The simplest way to resolve this conflict is to postulate an abundance ratio of Si to Al that differs from the one observed in the Sun. We find that an increase of ~ 0.4 dex in the relative abundance Si/Al (with respect to solar abundances) would ensure that the measured column density for Si II matches our prediction from the model solution. Similarly, our model overpredicts the S IV column density (traced by the pink curve). However, the measurement can be brought in complete agreement with our model with a decrease of ~ 0.35 dex in the relative abundance of S with respect to Al. The proposed changes for both Si/Al and S/Al abundance ratios are well within the ranges allowed by empirical abundance models in quasar outflows (Arav et al. 2013). Finally, Fig. 4 shows that our model solution satisfies the lower limit constraints (represented by dashed curves) from all ionic species except N V. We note that N V has an ionization potential (IP) of ~ 98 eV and is thus associated with a region with higher ionization than the other observed ionic species in our analysis which have IP $\lesssim 64$ eV. Observations of quasar outflows in the extreme UV have shown that when reliable column densities for higher ionization species (e.g., Ne VIII and Mg X) can be obtained,

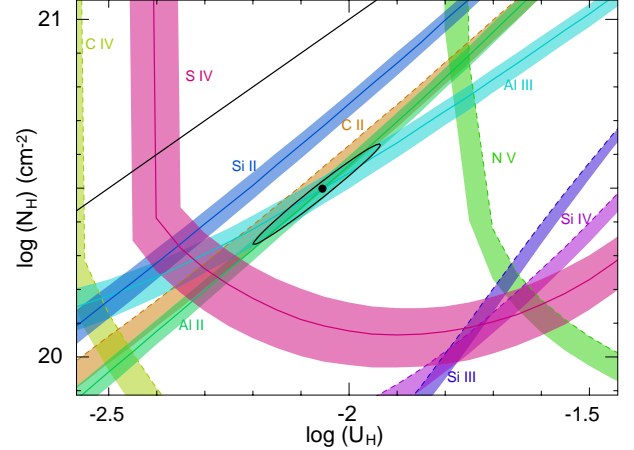


Figure 4. Plot of Hydrogen column density ($\log N_H$) vs. ionization parameter ($\log U_H$), with constraints based on the measured ionic column densities. Measurements are shown as solid curves, while the dashed curves show lower limits which allow the parameter space above them. The shaded regions denote the errors associated with each N_{ion} as reported in Table 2. The phase space solution with minimized χ^2 is shown as a black dot surrounded by a black ellipse indicating the $1\text{-}\sigma$ error. This solution is based on the N_{ion} of Al II and Al III (see section 2.2.3). The black line marks the position of the Hydrogen ionization front.

a single ionization phase is unable to provide an acceptable physical model for the outflow, thus requiring two distinct ionization phases (Arav et al. 2013, 2020). The high ionization species then correspond to a phase with higher N_H and U_H . From the VLT/X-shooter spectrum of 3C 191, we cannot obtain reliable measurements for column densities of other high ionization species, and therefore cannot constrain the high ionization phase completely. However, N V can still be ascribed to this phase, and that would explain why its N_{ion} constraint is not satisfied by our solution which represents the low ionization phase.

2.2.4. Electron Number Density

The ratios of the column densities of excited to resonance lines are an indicator of the electron number density (n_e) of an outflow under the assumption of collisional excitation (e.g., Arav et al. 2018). The identified outflow system in 3C 191 contains multiple troughs corresponding to the ground and excited states of Si II. As discussed in section 2.2.2, the Si II 1304 Å and Si II* 1309 Å transitions yield the most reliable measure of the column densities of Si II and Si II*. We obtain theoretical population ratios between the ground and excited state as a function of n_e using the CHIANTI atomic database (vers. 9.0 Dere et al. 1997, 2019).

A comparison of these theoretical predictions with the observed ratio of column densities of Si II* and Si II is shown in Fig. 5. This leads to $\log(n_e) = 2.78^{+0.08}_{-0.10}$ [cm^{-3}]. We also de-

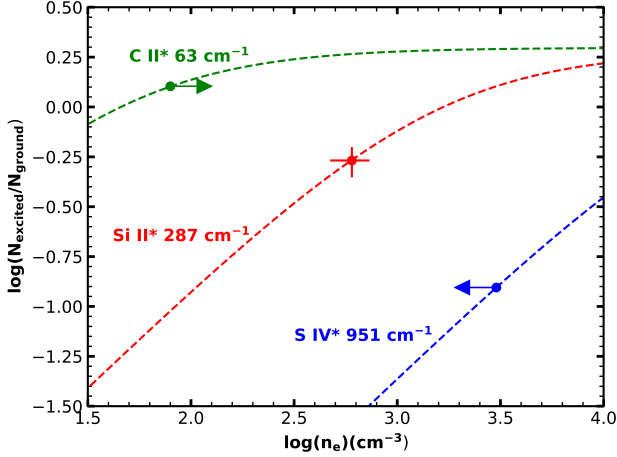


Figure 5. Dashed curves represent the theoretical population ratios for the transitions for an effective electron temperature $T_e = 8500$ K (determined from our CLOUDY modeling). The solid horizontal lines represent the observed column density ratios and their corresponding errors/limits.

tect C II 1335 Å and C II* 1336 Å transitions, which appear to be saturated and thus their AOD column densities will correspond to lower limits. Their ratio provides a lower limit of $\log(n_e) \geq 2.12_{-0.22}$ [cm^{-3}]. Although we do not detect the Si IV* 1073 Å trough, we use the Gaussian template obtained from the Si IV 1063 Å trough to obtain an upper limit for the column density of Si IV* based on its non-detection in the spectrum. The ratio of the Si IV* and Si IV column densities can then be used to determine an upper limit of $\log(n_e) \leq 3.38^{+0.10}$ [cm^{-3}]. Fig. 5 shows that the obtained upper and lower limits are in agreement with our n_e determined from Si II* and Si II population ratio.

2.3. Distance and Energetics

2.3.1. Distance Determination

Having determined U_H and n_e , we can use eqn. (3) to obtain the distance between the outflow and the central source (R) as:

$$R = \sqrt{\frac{Q_H}{4\pi U_H n_H c}} \quad (4)$$

Q_H can be obtained by integrating over the SED for energies above the Rydberg limit:

$$Q_H = \int_{\nu_{\text{Ryd}}}^{\infty} \frac{L_\nu}{h\nu} d\nu \quad (5)$$

The spectrum obtained from quasars with low-ionization absorption line outflows can be strongly affected by extinction due to dust in the host galaxy (Hall et al. 2002; Dunn et al. 2010; Leighly et al. 2024). To account for this reddening, we follow the methodology described by Hall et al.

(2002), which includes dereddening the spectrum until the continuum slope matches that of the composite SDSS quasar of Berk et al. (2001). In doing so, we find that the slope of the composite SDSS quasar matches that of the HE0238 SED for frequencies smaller than that of the Ly α line. The HE0238 SED is thus representative of a typical dereddened quasar spectrum. Therefore, to obtain the dereddened SED incident on the cloud, we scaled the HE0238 SED, by matching its flux to the observed flux from the VLT/X-shooter spectrum at an observed wavelength of $\lambda_{\text{obs}} = 10,000$ Å ($\lambda_{\text{rest}} = 3386.78$ Å). We chose the longest available wavelength for scaling as AGN extinction curves show that the extinction generally increases with increasing wavenumber, and is therefore smaller for longer wavelengths (Czerny et al. 2004; Gaskell et al. 2004). The resulting scaled SED is shown in blue in Fig. 6. The ionizing photons come from wavelengths shorter than the Lyman Limit which is not covered by VLT/X-shooter. Therefore to get a handle on the ionizing continuum we use the available CHANDRA observations of the object covering the 0.2-2 keV range, obtained from the second release of the Chandra Source Catalog (CSC). (Evans et al. 2010; Evans et al. 2020) The photometric flux measurements (converted to luminosity) are shown in the quasar rest frame in Fig. 6 as red points. The X-ray measurements are in agreement with the prediction from the scaled HE0238 SED, further strengthening our case for its use to model the incident flux on the cloud. Therefore, based on our scaled SED, we obtain $Q_H = 4.43^{+0.07}_{-0.07} \times 10^{56} \text{ s}^{-1}$ and Bolometric Luminosity $L_{\text{Bol}} = 8.00^{+0.13}_{-0.13} \times 10^{46} \text{ erg s}^{-1}$.

Typically, n_H is estimated from n_e under the assumption of highly ionized plasma, which leads to the approximation $n_e \approx 1.2n_H$. However, it has been shown that for the low ionization phases of the outflow, the formation of the hydrogen ionization front can lead to a sudden drop in n_e and therefore an underestimation for n_H (Sharma et al. 2025). We thus run a CLOUDY model for our outflow with $\log(n_H) = \log(n_e) = 2.78$ and the parameters obtained in section 2.2.3 and find that for this cloud, the hydrogen ionization front is not entirely developed, and thus while n_e deviates slightly from assumption of highly ionized plasma, the drop is not significant and an average over the cloud based on the zone-wise Si II column density yields $n_e \approx 1.1 n_H$. Substituting the determined values of Q_H , U_H and n_H into eqn. 4, we find that the outflow is located $5.1^{+0.9}_{-1.0}$ kpc away from the central source.

To obtain an estimate of the systematic error in the distance determination due to different SEDs, we check the difference between the Q_H and U_H determined from the HE0238 SED and the SED used by Hamann et al. (2001) in their Keck/HIRES analysis. The latter leads to a 25% increase in Q_H and a 7% decrease in U_H . Therefore, using eqn. (4), we can estimate the systematic error in our distance determination to be $\sim 16\%$.

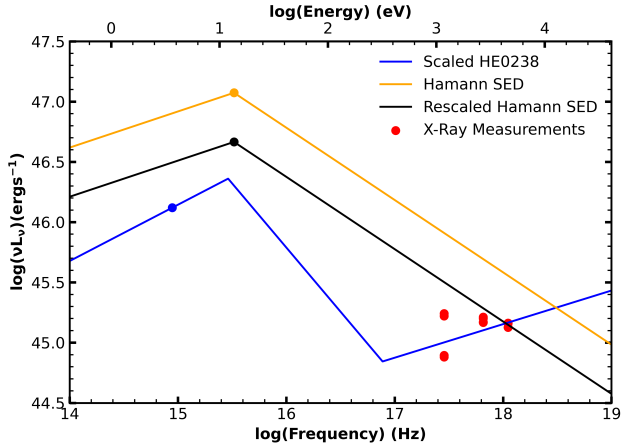


Figure 6. SEDs considered in the analysis. The blue curve corresponds to the scaled HE0238 SED, with the VLT/X-shooter flux used for scaling (at $\lambda_{obs} = 10000 \text{ \AA}$) given by the blue dot. The orange curve shows the SED used by Hamann et al. (2001) and the black curve shows the Hamann SED rescaled based on the VLT/X-shooter flux (see section 3.1 for more details). The red dots show the available X-ray flux measurements for the quasar. The error on these measurements are between 5% and 15% and thus comparable to or smaller than size of the points.

2.3.2. Energetics

The outflow can be modeled as a partial thin spherical shell covering a solid angle Ω , and moving with velocity v (Borguet et al. 2012b). The total mass of the gas within the outflow can then be obtained as:

$$M \simeq 4\pi\Omega R^2 N_H \mu m_p \quad (6)$$

where R is the spatial extent of the outflow, N_H is the total hydrogen column density, m_p is the proton mass, and $\mu = 1.4$ is the atomic weight of the plasma per proton. Defining the dynamic time scale as the time it takes the gas from the nucleus travelling at an average velocity v to reach the location of the outflow as $t_{dyn} = R/v$, we can obtain the mass loss rate \dot{M} and the kinetic luminosity \dot{E}_k of the outflow:

$$\dot{M} = \frac{M}{t_{dyn}} = 4\pi\Omega R N_H \mu m_p v \quad (7)$$

$$\dot{E}_k = \frac{1}{2} \dot{M} v^2$$

We assume $\Omega = 0.2$ based on the ratio of quasars that show a C IV BAL (Hewett & Foltz 2003). Using the velocity at the deepest absorption ($v = -720_{-12}^{+12} \text{ km s}^{-1}$) as the average velocity of the outflow leads to a mass loss rate of $\dot{M} = 33_{-12}^{+13} M_\odot \text{ yr}^{-1}$ and kinetic luminosity $\dot{E}_k = 5.5_{-2.0}^{+2.1} \times 10^{42} \text{ erg s}^{-1}$ for the outflow, which is $6.8_{-2.5}^{+2.7} \times 10^{-3} \%$ of L_{Bol} . This is much smaller than the $\gtrsim 0.5 \%$ required for efficient AGN feedback as determined by Hopkins & Elvis (2010).

3. REVISITING THE KECK-HIRES ANALYSIS OF HAMANN ET AL. (2001)

Hamann et al. (2001) observed 3C 191 using the High Resolution Echelle Spectrometer (HIRES) on the Keck I telescope on Mauna Kea, Hawaii. Using multiple observations adding up to 42,000 secs, they covered the wavelength range $\lambda \sim 3530 - 8927 \text{ \AA}$ with spectral resolution $R \approx 45,000$ and 3σ uncertainties $\lesssim 7\%$ for the final fluxes. Using the emission line redshift of $z = 1.956$ determined by Tytler & Fan (1992), they identified an outflow system covering a velocity range $-1400 \lesssim v \lesssim -400 \text{ km s}^{-1}$, with three components: $-1400 \lesssim \Delta v_1 \lesssim -1160 \text{ km s}^{-1}$, $-1160 \lesssim \Delta v_2 \lesssim -810 \text{ km s}^{-1}$ and $-810 \lesssim \Delta v_3 \lesssim -400 \text{ km s}^{-1}$. If we instead use the redshift determined by Zhao et al. (2025, in press.) ($z = 1.9527$), these components would have the velocities: $-1060 \lesssim \Delta v_1 \lesssim -820 \text{ km s}^{-1}$, $-820 \lesssim \Delta v_2 \lesssim -470 \text{ km s}^{-1}$ and $-470 \lesssim \Delta v_3 \lesssim -60 \text{ km s}^{-1}$. The outflow identified in the VLT/X-shooter spectrum (with $-950 \lesssim v \lesssim -500 \text{ km s}^{-1}$) is thus consistent with their system 2, which is their main outflow component, showing troughs from all species (see their Fig. 2 and Table 1). We can see their system 1 and 3 in the blue and red wings respectively of our troughs, but our Gaussian modeling is able to isolate the main component (see Fig. 2 and 3), thus allowing us to compare the results of their analysis with ours.

Hamann et al. (2001) analysed the outflow in great detail and estimated its radial distance to be $R \approx 28 \text{ kpc}$ from the central source. They determined $\log(U) \approx -2.8$ based on the comparison of the ratio of the Al II/Al III column densities to the theoretical ionization fractions in optically thin photoionized cloud using CLOUDY. They also utilized the ratio of the Si II $\lambda 1527 \text{ \AA}$ and Si II* $\lambda 1533 \text{ \AA}$ to obtain an estimate of the electron number density $n_e \approx 300 \text{ cm}^{-3}$ and assumed $n_H = n_e$. Finally, they modeled the ionizing spectrum as a power law with $L_\nu \propto \nu^\alpha$, where $\alpha = -1.6$ for frequencies above the Lyman limit, and $\alpha = -0.7$ below it (the orange curve in Fig. 6). Then they obtained the radial distance of the outflow using their equation (7):

$$R = \sqrt{\frac{-L_{LL}}{4\pi c n_H U \alpha}} \quad (8)$$

where $\alpha = -1.6$, h is the Planck constant and L_{LL} is the luminosity density at the Lyman Limit in the quasar rest frame, which was estimated by extrapolation of the data to the Lyman limit using the prescribed $\alpha = -0.7$, with $L_{LL} \approx 3.6 \times 10^{31} \text{ ergs s}^{-1} \text{ Hz}^{-1}$. This results in:

$$R = \sqrt{\frac{3.6 \times 10^{31}}{4\pi \cdot 2.998 \times 10^{10} \cdot 6.626 \times 10^{-27} \cdot 300 \cdot 10^{-2.8} \cdot 1.6}} \quad (9)$$

where all the values are in cgs units. This leads to $R \approx 1.38 \times 10^{23} \text{ cm} = 44.6 \text{ kpc}$. This is 1.6 times larger than their

reported value of $R \approx 28$ kpc obtained using the same parameters. Both these values are off by a factor of several when compared to the distance determined from our analysis of the VLT/X-shooter spectrum ($R \approx 5$ kpc), and therefore we take a detailed look at this discrepancy in the following sections.

3.1. Change in Continuum and Extrapolation to Lyman Limit

We compare the SED used by Hamann et al. (2001) with the scaled HE0238 SED used in our analysis in Fig. 6. This reveals that their νL_ν is roughly 6 times larger around the Lyman Limit. To understand this difference, we compare the observed spectrums obtained from both Keck/HIRES and VLT/X-shooter. At the longest available observed wavelength from their Fig. 1, $\lambda_{obs} \approx 4976$ Å, the measured flux density from the Keck/HIRES spectrum is $F_\lambda \approx 2.16 \times 10^{-16}$ and from the VLT/X-shooter spectrum is 0.91×10^{-16} [ergs cm⁻² s⁻¹ Å⁻¹]. A similar factor of increase in flux is also seen between the two spectrum at $\lambda_{obs} \approx 4000$ Å. Hence, while there is evidence for a change in continuum between these two epochs, it is much smaller than the difference seen in the SEDs. A likely reason for this could be the interpolation performed by Hamann et al. (2001) from their flux measurement at lower frequencies to the expected flux at Lyman Limit. The Keck/HIRES spectrum is limited on the short wavelength end by $\lambda_{rest} \gtrsim 1160$ Å and therefore their interpolation to shorter wavelengths is based on their power law index as discussed in the previous section. If we assume that the factor of increase in the continuum remains the same over the wavelength range, we can obtain an estimate for the Keck/HIRES flux at $\lambda_{obs} = 10,000$ Å as $F_\lambda \approx 1.09 \times 10^{-16}$ ergs cm⁻² s⁻¹ Å⁻¹. Using this to scale their SED gives us an estimate for L_{LL} for the Keck/HIRES spectrum, with $L_{LL} \approx 1.4 \times 10^{31}$ ergs s⁻¹ Hz⁻¹. This is roughly 40% of the estimate obtained by Hamann et al. (2001). The SED using the rescaled luminosity density is shown in Fig. 6 in black.

3.2. Photoionization modeling

Using the methodology described in section 2.2.3 we can obtain a photoionization model of the outflow. Hamann et al. (2001) determined a covering factor $C_f = 0.7$ for weak and intermediate lines, which they applied to the Al troughs to obtain their true column densities. They report the corrected total column densities for Al II and Al III integrated over all 3 velocity components, but we are interested primarily in their component 2 for which they do not report the corrections explicitly. However, we can note from their Fig. 2 that the Al II 1671 Å and Al III 1863 Å troughs have similar residual intensities at their deepest point with $I_r \approx 0.25$. Therefore any covering factor correction would affect them in the same way and would thus not significantly change their ratios, which is the indicator of the ionization state of the outflow. Therefore,

we use their determined column densities of $\log(N_{ion}) = 13.4$ and 14.0 [cm⁻²] for Al II λ 1671 Å and Al III λ 1863 Å respectively for component 2, with an assumed error of ± 0.1 dex based on the number of significant digits reported. We take the shape of the radiation incident upon the cloud to be the same as the power law SED of Hamann et al. (2001) and obtain the best-fit solution with $\log N_H = 20.72_{-0.20}^{+0.19}$ [cm⁻²] and $\log U_H = -2.09_{-0.19}^{+0.18}$. This N_H is roughly 1.7 times higher than our estimate from the VLT/X-shooter spectrum of $\log N_H = 20.50_{-0.16}^{+0.13}$ [cm⁻²]. The U_H based on their measurement is about 7 % lower than our estimate of $\log U_H = -2.06_{-0.14}^{+0.12}$ from the VLT spectrum, and is thus the same within the error bars. However, we note that this is ~ 5 times larger than the U determined by Hamann et al. (2001), who found $\log(U) \approx -2.8$. We perform CLOUDY simulations for an optically thin cloud and find that the ratio of Al II and Al III matches the observed ratio of column densities for $\log(U) = -2.8$. However, we also find that the assumption of the cloud being optically thin doesn't hold throughout our model. The ionic fractions for Al II, Al III and their ratio for a CLOUDY model with $\log N_H = 20.72$ [cm⁻²] and $\log U_H = -2.09$ are shown in Fig. 7. We find that the optical depth at the Lyman continuum τ_{LC} becomes greater than 1 for $N_H \gtrsim 10^{20}$ cm⁻² and the cloud is no longer optically thin. The ratio of the Al II and Al III ionic fractions therefore no longer remains constant, but instead increases as we approach the end of the cloud (the black curve in Fig. 7). As most of the contribution to the Al II and Al III population comes from these last zones, the average ratio for the cloud is significantly higher than that predicted by the assumption of the entire cloud being optically thin. Therefore the observed ratio of $N_{AlII}/N_{AlIII} \sim 10^{-0.6}$ is reproduced by a cloud with ionization parameter $\log U_H = -2.09$. The cloud with ionization parameter $\log U_H = -2.80$ on the other hand predicts $N_{AlII}/N_{AlIII} \sim 10^{0.2}$, which is contradicted by the observations.

3.3. Electron Number Density

Hamann et al. (2001) obtained the ratio of the Si II 1527 Å and Si II* 1533 Å to get an estimate of the electron number density as $n_e \approx 300$ cm⁻³, assuming a covering fraction $C_f = 0.7$. However we detect a much deeper Si II 1260 Å trough in the VLT/X-shooter spectrum, which indicates a higher covering fraction for Si II. At its deepest point, the Si II 1260 Å trough has residual intensity $I_r/I_0 \sim 0.1$. Equation (2) from Hamann et al. (2001) would thus suggest $C_f \geq 0.9$ for Si II. Such high values of C_f would make a constant covering factor correction negligible for the Si II troughs and therefore we consider $C_f = 1$. We also compare the Si II 1527 Å and Si II* 1533 Å troughs between the two epochs and find little variability for these troughs (see Fig. 8). We note that the Si II troughs seen in the Keck Spectrum were found to have a higher velocity than the VLT/X-Shooter spectrum by ~ 220

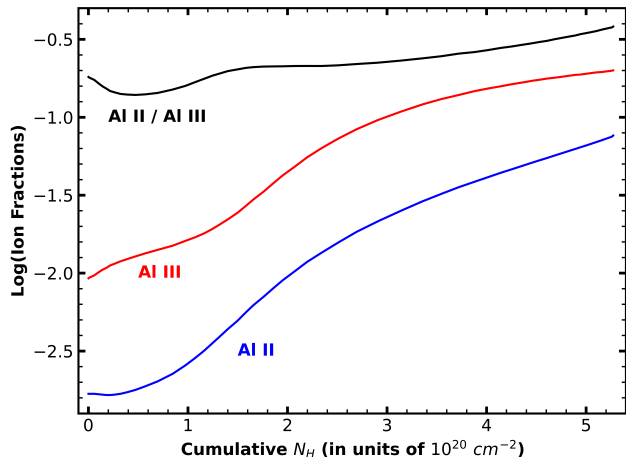


Figure 7. Ionic fraction within the cloud for $\log(U_H) = -2.09$. The blue and red curves shows the ionic fraction of Al II and Al III respectively, while the black curve shows their ratio.

km s^{-1} . The change in redshift from $z = 1.956$ to $z = 1.9527$ should result in a velocity shift of $\sim 340 \text{ km s}^{-1}$. Therefore, if we use the same redshift, there is an offset of $\sim 120 \text{ km s}^{-1}$ between the two spectra, which could be due to absolute wavelength calibration issues with the Keck spectrum.

Due to the lack of any significant variation, we can use our column density measurements for these troughs as they are the same as Hamann et al. (2001)’s determination to the third significant digit, and allow for error estimation based on our modeling, with $\log(N_{\text{Si II}}) = 14.59^{+0.02}_{-0.02} [\text{cm}^{-2}]$ and $\log(N_{\text{Si II}^*}) = 14.31^{+0.04}_{-0.04} [\text{cm}^{-2}]$. Following the steps described in section 2.2.4, we match the ratio of the column densities to the theoretical prediction from CHIANTI and obtain $n_e = 575^{+85}_{-74} \text{ cm}^{-3}$. This is in agreement with $n_e \approx 510 \text{ cm}^{-3}$ determined by Hamann et al. (2001) for $C_f = 1$. It is also in agreement with our determination of $n_e = 602^{+121}_{-124} \text{ cm}^{-3}$ from the Si II 1304 Å and Si II* 1309 Å troughs in the VLT/X-shooter spectrum.

Finally, We run a CLOUDY model for the outflow with the photoionization parameters obtained in section 3.2 and find that the hydrogen ionization front is not entirely developed, similar to our finding from the analysis of the VLT/X-shooter spectrum. Thus we find that averaging over the cloud based on the zone-wise Si II column density again yields $n_e \approx 1.1 n_H$.

3.4. Distance Determination

We have determined some changes in the values obtained for L_{LL} , U and n_e from the Keck/HIRES spectrum in our analysis so far in section 3. Using these updated values with eqn. (8), we find that the outflow is located $9.3^{+1.8}_{-2.5} \text{ kpc}$ away from the central source. This distance is $\sim 79 \%$ smaller than the earlier determination of $R \approx 44.6 \text{ kpc}$ based on the parameters reported in Hamann et al. (2001).

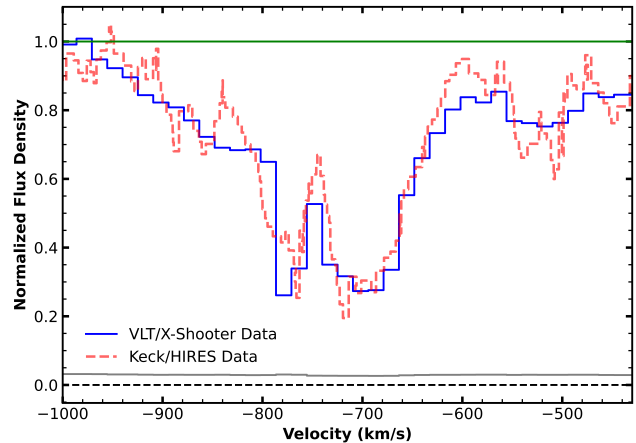


Figure 8. Comparison between the Si II 1527 Å trough obtained from the VLT/X-shooter spectrum (blue) and the Keck/HIRES spectrum (red). The Keck/HIRES spectrum was shifted in velocity space to match the troughs for this comparison. The green line shows the local continuum level, and the gray line shows the noise in the VLT/X-shooter flux.

However, as we discussed in section 2.3.1, the HE0238 SED is a better representative of the shape of the radiation incident upon the cloud. Therefore we scale it to the expected Keck/HIRES flux at $\lambda_{\text{obs}} = 10,000 \text{ Å}$ determined in section 3.1. This leads to $Q_H = 1.1 \times 10^{57} \text{ s}^{-1}$. We also use the HE0238 SED in the photoionization modeling with the Al column densities determined by Hamann et al. (2001) and find that it decreases the required ionization parameter to $\log U_H = -2.13^{+0.16}_{-0.18}$. Using these updated values with eqn. (4) puts the outflow at a distance $R = 8.9^{+1.4}_{-2.7} \text{ kpc}$ away from the central source. This updated analysis brings the distance determined from the Keck/HIRES spectrum much closer to our estimate of $5.1^{+0.9}_{-1.0} \text{ kpc}$ based on the VLT/X-shooter spectrum. The difference between these two distance estimates stems mostly from the difference in Q_H which is due to the flux difference between the two spectra. If the Keck/HIRES spectrum is scaled to match the continuum level of the VLT/X-Shooter spectrum, the distance of the outflow determined from the Keck/HIRES spectrum would have been $R = 5.8^{+1.2}_{-1.5} \text{ kpc}$, which is in good agreement with our distance determination from VLT/X-shooter spectrum. We discuss the issues concerning this flux difference in section 5.1.

4. COMPARISON WITH THE IFS ANALYSIS

3C 191 was also observed by the Spectrograph for INtegral Field Observations in the Near Infrared (SINFONI) on VLT in multiple sessions between December 2017 and March 2018 (as part of program: 097.B-0570(B), PI: Benn) with a total integration time of 4800 s. The observations covered a rest-frame spectral range of 4910-6266 Å, with spectral resolution of $R = 3000$, and angular resolution of $0.24'' \times 0.24''$, which corresponds to a spatial resolution of $\sim 2 \times 2 \text{ kpc}$ at

the redshift of the quasar. In our companion paper (Zhao et al. 2025, in press.) we analysed the ionized outflow in emission as traced by the [O III] $\lambda\lambda$ 4959, 5007 doublet. The [O III] line profile is decomposed into three distinct velocity components: blueshifted, zero velocity and redshifted with respect to the quasar. The zero velocity component is consistent with a typical narrow line region for the quasar, while the blueshifted/redshifted components show strong signs of a bipolar outflow (see section 4 of Zhao et al. 2025, in press., for a detailed description of the extended emission line features). For comparison with the outflow detected in absorption, we focus on the blueshifted component of the emission outflow.

The blueshifted outflow component seen in emission covers a velocity range $-1090 \lesssim v \lesssim -20 \text{ km s}^{-1}$. This is consistent with the outflow seen in absorption in the VLT/X-shooter spectrum spanning velocity range $-950 \lesssim v \lesssim -250 \text{ km s}^{-1}$. This includes the main absorption system analysed in this paper and its blue wing as seen in Figs. 2 and 3. This kinematic correspondence between the outflows seen in absorption and emission thus suggests a common origin for them. Furthermore, the projected distance determined from the IFS mapping for the blueshifted outflow component is $R \sim 5 \text{ kpc}$ (Fig. 9). This is in remarkable agreement with the indirect distance determination of $R = 5.1^{+0.9}_{-1.0} \text{ kpc}$ obtained for the outflow based on the absorption analysis detailed in section 2.3.1. This is the first instance where independent emission and absorption analysis of a quasar outflow have yielded consistent values for the distance of the outflow from the central source. While comparing the distances between our absorption and IFS analyses, it is important to note that they do not inherently measure the same distance. The absorption analysis measures the distance of the outflowing component from the central source along our line-of-sight, whereas the IFS analysis measures the projected distance in the sky plane. The relation between these two distance depends upon the geometry of the outflow. Fig. 9 (along with others in Zhao et al. (2025, in press.)) hints towards a roughly spherically symmetric outflow, in which case the line-of-sight distance and the projected distance in the sky plane would be similar. However, other geometries for the outflow (such as bi-polar) cannot be clearly ruled out on the basis of Fig. 9 alone.

Zhao et al. (2025, in press.) also estimate the energetics for the IFS manifestation of the outflow (see their section 5.2 for a detailed description). The mass of the ionized gas is estimated using the [O III] luminosity, using the n_e determined from our absorption analysis. The mass loss rate (\dot{M}) and the kinetic luminosity (\dot{E}_{kin}) are then calculated accordingly, with the results summarized in Table 3. The energetics from the absorption analysis and the IFS analysis are consistent within a factor of 3, with the difference arising mostly due to the smaller M_{gas} obtained for the IFS analysis. We note that

the ionized gas mass obtained from the emission lines suffer from greater uncertainties than their absorption counterpart due to several factors, such as the temperature dependence of line emissivities. Moreover, as Carniani et al. (2015) show, the ionized gas mass traced by [O III] is usually lower than that traced by $H\beta$, which was not covered in the observations analysed by Zhao et al. (2025, in press.).

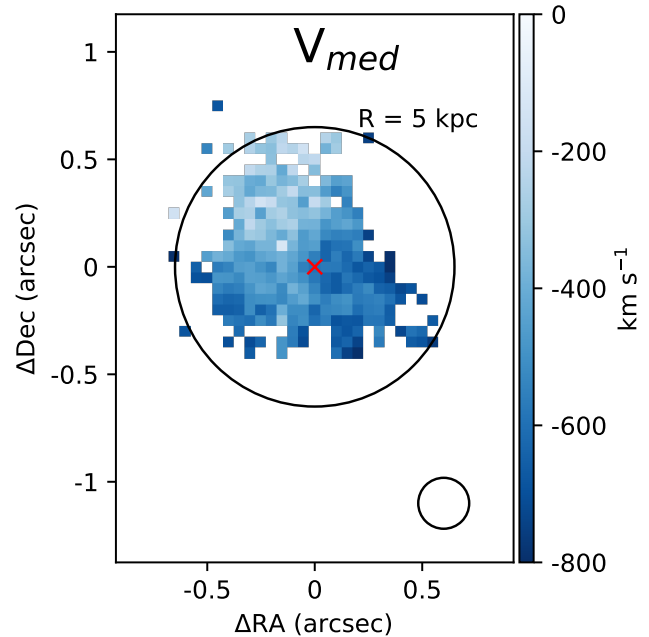


Figure 9. Median velocity map of the blueshifted component of the ionized outflow seen in emission. The red cross marks the position of the quasar and the smaller open circle depicts the point-spread function (PSF). The $R = 5 \text{ kpc}$ boundary centered around the quasar is shown by the bigger black circle.

5. DISCUSSION

5.1. Variability of the central source

As discussed in section 3.4, the difference between the distance estimates obtained from the Keck/HIRES (1997 epoch) and the VLT/X-shooter (2013 epoch) analyses can be traced solely to a factor of ~ 2.4 flux difference between the two spectra. During this period, 3C 191 was also observed by the Catalina Real-time Transient Survey (CRTS; Drake et al. 2009) between April 2005 and October 2013. It was also observed later by the Zwicky Transient Facility (ZTF; Bellm et al. 2018; Malanchev et al. 2023) between March 2018 and February 2023. Over the combined ~ 15 years of observation, the quasar showed little variability in flux ($\lesssim 20\%$) in all the observed bands.

Moreover, equation (3) suggests that variation in the ionizing flux should lead to a change in the ionization state of the gas given that the timescale of flux variation is comparable

Table 3. Kinematics and Energetics for the outflow in 3C 191

Parameter	Absorption	IFS
	Value	Value
v (km s ⁻¹)	-950 to -500	-1090 to -20
R (kpc)	$5.1^{+0.9}_{-1.0}$	$5^{+1.3}_{-0.2}$
t_{dyn} (yrs)	$6.9^{+1.2}_{-1.3} \times 10^6$	$5.0^{+0.3}_{-0.3} \times 10^6$
M_{gas} (M_{\odot})	$2.3^{+1.1}_{-1.1} \times 10^8$	$6.6^{+0.7}_{-0.7} \times 10^7$
\dot{M} (M_{\odot} yr ⁻¹)	33^{+13}_{-12}	9.5-13.4
E_{kin} (erg)	$1.2^{+0.6}_{-0.6} \times 10^{57}$	$5.3^{+0.9}_{-0.9} \times 10^{56}$
\dot{E}_{kin} (erg s ⁻¹)	$5.5^{+2.1}_{-2.0} \times 10^{42}$	$2.6\text{-}3.7 \times 10^{42}$

NOTE—The reported values for the absorption analysis are only for the main component and does not include contribution from the associated absorption in the blue wing. For the IFS analysis, the reported kinematics are for the blueshifted component, whereas the energetics correspond to the blueshifted + redshifted component that make up the outflowing bubble.

to the recombination timescale of the gas. For an absorber in photoionization equilibrium, if there is a sudden change of order unity in the incident ionizing flux, the timescale for the change in the ionic fraction of a species is given by (Krolik & Kriss 1996; Arav et al. 2012):

$$t^* = \left[\alpha_i n_e \left(\frac{n_{i+1}}{n_i} - \frac{\alpha_{i-1}}{\alpha_i} \right) \right]^{-1}, \quad (10)$$

where n_e is the electron number density of the gas, α_i is the recombination rate of the ion i and n_i is the fraction of a given element in ionization stage i . For the last zone of our modeled cloud, we can obtain n_e , n_i and α_i from CLOUDY. The timescales for change in ionic fractions of Si II, Al II and Al III can then be determined using eqn. (10), resulting in $t_{Si II}^* \sim 1$ yr, $t_{Al II}^* \sim 3$ yrs and $t_{Al III}^* \sim 31$ yrs. This suggests that a change in the ionizing flux from the quasar over a timescale $t \gtrsim 1$ yr would have led to a change in the observed troughs of Si II and Al II. However as shown in Fig. 8, no significant change is seen in these troughs between the two epochs. This is consistent with the observations from CRTS and ZTF, and therefore the large difference in the flux seen between the Keck/HIRES and VLT/X-shooter spectra is unlikely to be a result of intrinsic flux variation in the quasar. There could thus be possible issues with the absolute flux-calibration for these observations.

5.2. Comparison with other outflows

Liu et al. (2015) obtained the IFS maps of two Seyfert 1.5 galaxies: IRAS F04250-5718 and Mrk 509 using the

Gemini Multi-Object Spectrograph (GMOS) on the Gemini South telescope (program ID: GS-2013B-Q-84, PI: D. Rupke). Both these objects were already known to have shown outflows in absorption for which indirect distance constraints were available. Liu et al. (2015) detected ionized outflows in emission for both objects as traced by the [O III] $\lambda\lambda$ 4959, 5007 doublet, and thus presented one of the first such comparisons between AGN outflows analysed using absorption and IFS techniques. Here we summarize the results of these analyses in brief.

IRAS F04250-5718: Liu et al. (2015) detected a bi-conical outflow extending out to ~ 2.2 kpc on one side and ~ 2.9 kpc on the other. They determined the maximum line-of-sight velocity of the the outflowing gas to be $\sim 330 \pm 30$ km s⁻¹ based on modifications to the spherical outflow model of Liu et al. (2013), in which the opening angle of the outflow is measured to be $\sim 70^\circ$ as per their IFS map of [O III] linewidth. Analysis of the outflow seen in absorption in this object was performed by Edmonds et al. (2011) based on high-resolution data obtained from the Cosmic Origins Spectrograph (COS) on the Hubble Space Telescope (HST). They identified three different kinematic components spanning velocity range $-290 \lesssim v \lesssim +30$ km s⁻¹. Based on the non-detection of excited states from C II, they derived an upper limit on the electron number density of the outflow with $n_e \lesssim 30$ cm⁻³. This provided a constraint on the distance of the outflow from the central source and placed it at-least 3 kpc away ($R \gtrsim 3$ kpc). This is consistent with the spatial extent of the outflow on one side of the quasar.

Mrk 509: The outflow detected from the IFS mapping by Liu et al. (2015) shows a roughly spherical morphology with a radius of ~ 1.2 kpc, and velocity $v \sim 293 \pm 51$ km s⁻¹. On the absorption front, Kraemer et al. (2003) obtained Space Telescope Imaging Spectrograph (STIS) echelle spectrum of the AGN. Mrk 509 was also the subject of a large multi-wavelength campaign (Kaastra et al. 2011) as part of which it was observed with HST/COS. Kriss et al. (2011) identified nine absorption systems spanning velocity range $-425 \lesssim v \lesssim +250$ km s⁻¹. Comparison between the C IV and N V troughs seen in the STIS and COS spectrums showed negligible variation despite a large change in the ionizing flux. This allowed them to obtain upper limits on the electron number densities based on recombination timescale arguments. Using this, they determined a lower limit on the distance to the absorber of 100-200 pc from the ionizing source for all the components, which is again consistent with the spatial extent of the outflow determined from the IFS mapping (~ 1.2 kpc).

Therefore, the IFS analysis of both these objects revealed that the spatial extent of the outflows were consistent with the constraints determined from the indirect determination. However, as the absorption analysis only provided lower limits on the indirect distance determination, a conclusive corre-

spondence can not be drawn between the distances obtained from the two techniques. Therefore, a direct quantitative comparison of the absorption and emission techniques is featured for the first time in this work and our companion paper Zhao et al. (2025, in press.).

6. SUMMARY

This paper (along with the companion paper by Zhao et al. 2025, in press.) presents a detailed study of the ionized outflow associated with the radio-loud quasar 3C 191 using absorption and IFS analysis techniques. In the VLT/X-Shooter spectrum of the quasar, we identify an outflow system in absorption with velocity $v \sim -720 \text{ km s}^{-1}$. We detect multiple ionized species covering a broad range of ionization and model the observed troughs to obtain their column densities (Section 2.2.2). We then obtain the best fit photoionization model for the cloud with total hydrogen column density $\log N_H = 20.50^{+0.13}_{-0.16} [\text{cm}^{-2}]$ and ionization parameter $\log U_H = -2.06^{+0.12}_{-0.14}$ based on the observed Al II and Al III column densities (Section 2.2.3). The detection of the metastable excited state of Si II allows us to obtain the electron number density of the outflow with $\log n_e = 2.78^{+0.08}_{-0.10} [\text{cm}^{-3}]$ (Section 2.2.4). Combining these parameters with our informed assumption for the incident SED (Fig. 6) locates the outflow at a distance of $R = 5.1^{+0.9}_{-1.0} \text{ kpc}$ from the central source. This leads to a mass loss rate of $\dot{M} = 33^{+13}_{-12} M_\odot \text{ yr}^{-1}$ and kinetic luminosity $\dot{E}_k = 5.5^{+2.1}_{-2.0} \times 10^{42} \text{ erg s}^{-1}$ for the outflow.

We note that our distance determination from the VLT/X-Shooter spectrum is in disagreement with that of Hamann et al. (2001) who analysed the Keck/HIRES spectrum of 3C 191 and placed the outflow at a much larger distance of $R \sim 28 \text{ kpc}$. We revisit their analysis in section 3 and obtain different values for the number of ionizing photons (Q_H) and the ionization parameter (U_H) based on our analysis tech-

niques detailed in section 3.1 and 3.2 respectively. This leads to an updated value for the distance determined from the Keck/HIRES spectra with $R = 8.9^{+1.4}_{-2.7} \text{ kpc}$, which is much closer to our estimate from the VLT/X-Shooter spectrum.

Zhao et al. (2025, in press.) details our analysis of the spatially-resolved integral field observations of the ionized outflow surrounding 3C 191 obtained using VLT/SINFONI. In section 4, we compare the properties of the [O III] outflow seen in emission with the outflow detected in absorption. These two independent approaches lead to a remarkably consistent picture for the outflow as the distance determined indirectly using absorption analysis is verified by the spatial extent of the outflow determined directly from the IFS observations for the first time for a quasar outflow. The kinematics and energetics of the two manifestations of the outflow are also found to be in agreement as shown in Table 3.

1 We acknowledge support from NSF grant AST 2106249,
2 as well as NASA STScI grants AR-15786, AR-16600, AR-
3 16601 and AR-17556. Q.Z., L.S. and G.L. acknowledge the
4 support from the China Manned Space Project (the second-
5 stage CSST science project: *Investigation of small-scale*
6 *structures in galaxies and forecasting of observations*, Nos.
7 CMS-CSST-2021-A06 and CMS-CSST-2021-A07), the National
8 Natural Science Foundation of China (No. 12273036),
9 the Ministry of Science and Technology of China (No.
10 2023YFA1608100), and the Cyrus Chun Ying Tang Founda-
11 tions. Q.Z. and J.W. acknowledge National Natural Science
12 Foundation of China (NSFC) grants 12033004, 12333002.
13 Q.Z. acknowledges the support from the China Postdoc-
14 toral Science Foundation (2023M732955). We also thank
15 the anonymous referee for their constructive comments that
16 helped improve this paper.

REFERENCES

- Akujor, C. E., Lüdke, E., Browne, I., et al. 1994, *Astronomy and Astrophysics Suppl.*, Vol. 105, p. 247-258 (1994), 105, 247
- Alexander, D., Swinbank, A., Smail, I., McDermid, R., & Nesvadba, N. 2010, *Monthly Notices of the Royal Astronomical Society*, 402, 2211
- Aoki, K., Oyabu, S., Dunn, J. P., et al. 2011, *Publications of the Astronomical Society of Japan*, 63, S457
- Arav, N., Borguet, B., Chamberlain, C., Edmonds, D., & Danforth, C. 2013, *Monthly Notices of the Royal Astronomical Society*, 436, 3286
- Arav, N., Kaastra, J., Kriss, G. A., et al. 2005, *The Astrophysical Journal*, 620, 665
- Arav, N., Korista, K. T., de Kool, M., Junkkarinen, V. T., & Begelman, M. C. 1999, *The Astrophysical Journal*, 516, 27
- Arav, N., Liu, G., Xu, X., et al. 2018, *The Astrophysical Journal*, 857, 60
- Arav, N., Xu, X., Miller, T., Kriss, G. A., & Plesha, R. 2020, *The Astrophysical Journal Supplement Series*, 247, 37
- Arav, N., Edmonds, D., Borguet, B., et al. 2012, *Astronomy & Astrophysics*, 544, A33
- Bahcall, J. N., Sargent, W. L., & Schmidt, M. 1967, *Astrophysical Journal*, vol. 149, p. L11, 149, L11
- Baron, D., & Netzer, H. 2019, *Monthly Notices of the Royal Astronomical Society*, 486, 4290
- Bautista, M. A., Dunn, J. P., Arav, N., et al. 2010, *The Astrophysical Journal*, 713, 25

- Bellm, E. C., Kulkarni, S. R., Graham, M. J., et al. 2018, *Publications of the Astronomical Society of the Pacific*, 131, 018002
- Berk, D. E. V., Richards, G. T., Bauer, A., et al. 2001, *The Astronomical Journal*, 122, 549
- Bischetti, M., Choi, H., Fiore, F., et al. 2024, arXiv preprint arXiv:2404.12443
- Borguet, B. C., Arav, N., Edmonds, D., Chamberlain, C., & Benn, C. 2012a, *The Astrophysical Journal*, 762, 49
- Borguet, B. C., Edmonds, D., Arav, N., Dunn, J., & Kriss, G. A. 2012b, *The Astrophysical Journal*, 751, 107
- Burbidge, E., Lynds, C., & Burbidge, G. 1966, *Astrophysical Journal*, vol. 144, p. 447, 144, 447
- Byun, D., Arav, N., Dehghanian, M., Walker, G., & Kriss, G. A. 2024a, *Monthly Notices of the Royal Astronomical Society*, 529, 3550
- Byun, D., Arav, N., & Hall, P. B. 2022a, *Monthly Notices of the Royal Astronomical Society*, 517, 1048
- Byun, D., Arav, N., Sharma, M., Dehghanian, M., & Walker, G. 2024b, *Astronomy & Astrophysics*, 684, A158
- Byun, D., Arav, N., & Walker, A. 2022b, *Monthly Notices of the Royal Astronomical Society*, 516, 100
- Carniani, S., Marconi, A., Maiolino, R., et al. 2015, *Astronomy & Astrophysics*, 580, A102
- Cattaneo, A., Faber, S., Binney, J., et al. 2009, *Nature*, 460, 213
- Chamberlain, C., & Arav, N. 2015, *Monthly Notices of the Royal Astronomical Society*, 454, 675
- Chamberlain, C., Arav, N., & Benn, C. 2015, *Monthly Notices of the Royal Astronomical Society*, 450, 1085
- Chatzikos, M., Bianchi, S., Camilloni, F., et al. 2023, *RMxAA*, 59, 327, doi: [10.22201/ia.01851101p.2023.59.02.12](https://doi.org/10.22201/ia.01851101p.2023.59.02.12)
- Czerny, B., Li, J., Loska, Z., & Szczerba, R. 2004, *Monthly Notices of the Royal Astronomical Society*, 348, L54
- Davé, R., Anglés-Alcázar, D., Narayanan, D., et al. 2019, *Monthly Notices of the Royal Astronomical Society*, 486, 2827
- Davidson, K., & Netzer, H. 1979, *Reviews of Modern Physics*, 51, 715
- Davies, R., Baron, D., Shimizu, T., et al. 2020, *Monthly Notices of the Royal Astronomical Society*, 498, 4150
- de Kool, M., Arav, N., Becker, R. H., et al. 2001, *The Astrophysical Journal*, 548, 609
- Dehghanian, M., Arav, N., Byun, D., Walker, G., & Sharma, M. 2024, *Monthly Notices of the Royal Astronomical Society*, 527, 7825
- Dere, K., Landi, E., Mason, H., Fossi, B. M., & Young, P. 1997, *Astronomy and Astrophysics Supplement Series*, 125, 149
- Dere, K. P., Del Zanna, G., Young, P. R., Landi, E., & Sutherland, R. S. 2019, *The Astrophysical Journal Supplement Series*, 241, 22
- Donnari, M., Pillepich, A., Joshi, G. D., et al. 2021, *Monthly Notices of the Royal Astronomical Society*, 500, 4004
- Drake, A., Djorgovski, S., Mahabal, A., et al. 2009, *The Astrophysical Journal*, 696, 870
- Dubois, Y., Devriendt, J., Slyz, A., & Teyssier, R. 2012, *Monthly Notices of the Royal Astronomical Society*, 420, 2662
- Dunn, J. P., Bautista, M., Arav, N., et al. 2010, *The Astrophysical Journal*, 709, 611
- Edmonds, D., Borguet, B., Arav, N., et al. 2011, *The Astrophysical Journal*, 739, 7
- Evans, I. N., Primini, F. A., Glotfelty, K. J., et al. 2010, *The Astrophysical Journal Supplement Series*, 189, 37
- Evans, I. N., Primini, F. A., Miller, J. B., et al. 2020, in *American Astronomical Society Meeting Abstracts*, Vol. 235, *American Astronomical Society Meeting Abstracts #235*, 154.05
- Finn, C. W., Morris, S. L., Crighton, N. H., et al. 2014, *Monthly Notices of the Royal Astronomical Society*, 440, 3317
- Gaskell, C. M., Goosmann, R. W., Antonucci, R. R., & Whysong, D. H. 2004, *The Astrophysical Journal*, 616, 147
- Hall, P. B., Anderson, S. F., Strauss, M. A., et al. 2002, *The Astrophysical Journal Supplement Series*, 141, 267
- Hamann, F., & Sabra, B. 2004, in *Astronomical Society of the Pacific Conference Series*, Vol. 311, *AGN Physics with the Sloan Digital Sky Survey*, 203, doi: [10.48550/arXiv.astro-ph/0310668](https://doi.org/10.48550/arXiv.astro-ph/0310668)
- Hamann, F. W., Barlow, T., Chaffee, F., Foltz, C., & Weymann, R. 2001, *The Astrophysical Journal*, 550, 142
- Harrison, C., Alexander, D., Mullaney, J., & Swinbank, A. 2014, *Monthly Notices of the Royal Astronomical Society*, 441, 3306
- Harrison, C., Alexander, D., Swinbank, A., et al. 2012, *Monthly Notices of the Royal Astronomical Society*, 426, 1073
- He, Z., Liu, G., Wang, T., et al. 2022, *Science Advances*, 8, eabk3291
- Hewett, P. C., & Foltz, C. B. 2003, *The Astronomical Journal*, 125, 1784
- Hlavacek-Larrondo, J., Li, Y., & Churazov, E. 2024, in *Handbook of X-ray and Gamma-ray Astrophysics* (Springer), 4895–4960
- Holt, J., Tadhunter, C., Morganti, R., & Emons, B. 2011, *Monthly Notices of the Royal Astronomical Society*, 410, 1527
- Hopkins, P. F., & Elvis, M. 2010, *Monthly Notices of the Royal Astronomical Society*, 401, 7
- Kaastra, J., Petrucci, P.-O., Cappi, M., et al. 2011, *Astronomy & Astrophysics*, 534, A36
- Kakkad, D., Mainieri, V., Vietri, G., et al. 2020, *Astronomy & Astrophysics*, 642, A147
- Karouzos, M., Woo, J.-H., & Bae, H.-J. 2016, *The Astrophysical Journal*, 819, 148
- Kim, C., Woo, J.-H., Luo, R., et al. 2023, *The Astrophysical Journal*, 958, 145
- Kraemer, S., Crenshaw, D., Yaqoob, T., et al. 2003, *The Astrophysical Journal*, 582, 125

- Kriss, G., Arav, N., Kaastra, J., et al. 2011, *Astronomy & Astrophysics*, 534, A41
- Krolik, J., & Kriss, G. 1996, *Astrophysical Journal* v. 456, p. 909, 456, 909
- Krolik, J. H. 1999, *Active galactic nuclei: from the central black hole to the galactic environment*, Vol. 59 (Princeton University Press)
- Leighly, K. M., Choi, H., Eracleous, M., et al. 2024, arXiv preprint arXiv:2402.07855
- Liu, G., Arav, N., & Rupke, D. S. 2015, *The Astrophysical Journal Supplement Series*, 221, 9
- Liu, G., Zakamska, N. L., & Greene, J. E. 2014, *Monthly Notices of the Royal Astronomical Society*, 442, 1303
- Liu, G., Zakamska, N. L., Greene, J. E., Nesvadba, N. P., & Liu, X. 2013, *Monthly Notices of the Royal Astronomical Society*, 436, 2576
- Lucy, A. B., Leighly, K. M., Terndrup, D. M., Dietrich, M., & Gallagher, S. C. 2014, *The Astrophysical Journal*, 783, 58
- Malanchev, K., Kornilov, M. V., Pruzhinskaya, M. V., et al. 2023, *Publications of the Astronomical Society of the Pacific*, 135, 024503
- Miller, T. R., Arav, N., Xu, X., Kriss, G. A., & Plesha, R. J. 2020, *The Astrophysical Journal Supplement Series*, 247, 41
- Miller, T. R., Arav, N., Xu, X., et al. 2018, *The Astrophysical Journal*, 865, 90
- Modigliani, A., Goldoni, P., Royer, F., et al. 2010, in *Observatory operations: Strategies, processes, and systems iii*, Vol. 7737, SPIE, 572–583
- Moe, M., Arav, N., Bautista, M. A., & Korista, K. T. 2009, *The Astrophysical Journal*, 706, 525
- Nesvadba, N., Lehnert, M. D., De Breuck, C., Gilbert, A., & Van Breugel, W. 2008, *Astronomy & Astrophysics*, 491, 407
- Noterdaeme, P., Balashev, S., Krogager, J.-K., et al. 2021, *Astronomy & Astrophysics*, 646, A108
- Osterbrock, D. E., & Ferland, G. J. 2006, *Astrophysics Of Gas Nebulae and Active Galactic Nuclei* (University science books)
- Parlanti, E., Carniani, S., Übler, H., et al. 2024, *A&A*, 684, A24, doi: [10.1051/0004-6361/202347914](https://doi.org/10.1051/0004-6361/202347914)
- Pearson, T., Perley, R., & Readhead, A. 1985, *Astronomical Journal* (ISSN 0004-6256), vol. 90, May 1985, p. 738-755., 90, 738
- Planck Collaboration, Aghanim, N., Akrami, Y., et al. 2020, *A&A*, 641, A6, doi: [10.1051/0004-6361/201833910](https://doi.org/10.1051/0004-6361/201833910)
- Rupke, D. S., & Veilleux, S. 2011, *The Astrophysical Journal Letters*, 729, L27
- . 2013, *The Astrophysical Journal*, 768, 75
- Savage, B. D., & Sembach, K. R. 1991, *The Astrophysical Journal*, 379, 245
- Sharma, M., Arav, N., Korista, K. T., et al. 2025, *Astronomy & Astrophysics*, 693, A254
- Shen, L., Liu, G., He, Z., et al. 2023, *Science Advances*, 9, eadg8287
- Silk, J., & Mamon, G. A. 2012, *Research in Astronomy and Astrophysics*, 12, 917
- Stockton, A., & Lynds, C. 1966, *Astrophysical Journal*, vol. 144, p. 451, 144, 451
- Travascio, A., Piconcelli, E., Bischetti, M., et al. 2024, *Astronomy & Astrophysics*, 686, A250
- Tytler, D., & Fan, X.-M. 1992, *Astrophysical Journal Supplement Series* (ISSN 0067-0049), vol. 79, March 1992, p. 1-36., 79, 1
- Übler, H., D'Eugenio, F., Perna, M., et al. 2024, *Monthly Notices of the Royal Astronomical Society*, stae1993
- Vernet, J., Dekker, H., d'Odorico, S., et al. 2011, *Astronomy & Astrophysics*, 536, A105
- Walker, A., Arav, N., & Byun, D. 2022, *Monthly Notices of the Royal Astronomical Society*, 516, 3778
- Williams, R., Strittmatter, P., Carswell, R., & Craine, E. 1975, *Astrophysical Journal*, vol. 202, Dec. 1, 1975, pt. 1, p. 296-302., 202, 296
- Wylezalek, D., Flores, A. M., Zakamska, N. L., Greene, J. E., & Riffel, R. A. 2020, *Monthly Notices of the Royal Astronomical Society*, 492, 4680
- Xu, X., Arav, N., Miller, T., & Benn, C. 2018, *The Astrophysical Journal*, 858, 39
- . 2019, *The Astrophysical Journal*, 876, 105
- Xu, X., Arav, N., Miller, T., Korista, K. T., & Benn, C. 2021, *Monthly Notices of the Royal Astronomical Society*, 506, 2725
- Xu, X., Arav, N., Miller, T., Kriss, G. A., & Plesha, R. 2020, *The Astrophysical Journal Supplement Series*, 247, 42
- Zhao, Q., Sun, L., Liu, G., et al. 2025, in press.
- Zhao, Q., & Wang, J. 2023, *The Astrophysical Journal Letters*, 943, L25

APPENDIX

A. MULTIPLE COMPONENT MODELING OF THE ABSORPTION TROUGHS

While determining the column densities for the outflowing system in section 2.2.2, we model the troughs with a single Gaussian. However, as Fig. 2 and 3 show, the absorption troughs of Al III, Al II and Si II show additional absorption in their wings. These components are not the focus of our analysis in this work as they do not show corresponding absorption for Si II*. However, to ensure that they do not affect our column density measurement for the main component, we perform a multiple component Gaussian fit for the entire absorption feature. We detail the fitting procedure for Al II/III and Si II separately below.

A.1. Details of the Models.

A.1.1. Al

We first model the Al III 1863 Å trough with two independent Gaussian profiles for optical depth. We then use this model as a template for the Al III 1855 Å and Al II 1671 Å troughs by fixing the centroid and width of both Gaussians while allowing their depth to vary independently. In the case of Al II 1671 Å, we allow for an additional component to model the absorption blend in the red wing. The results for the best-fit model templates (determined by non-linear least squares) for these troughs are shown in Fig. 10.

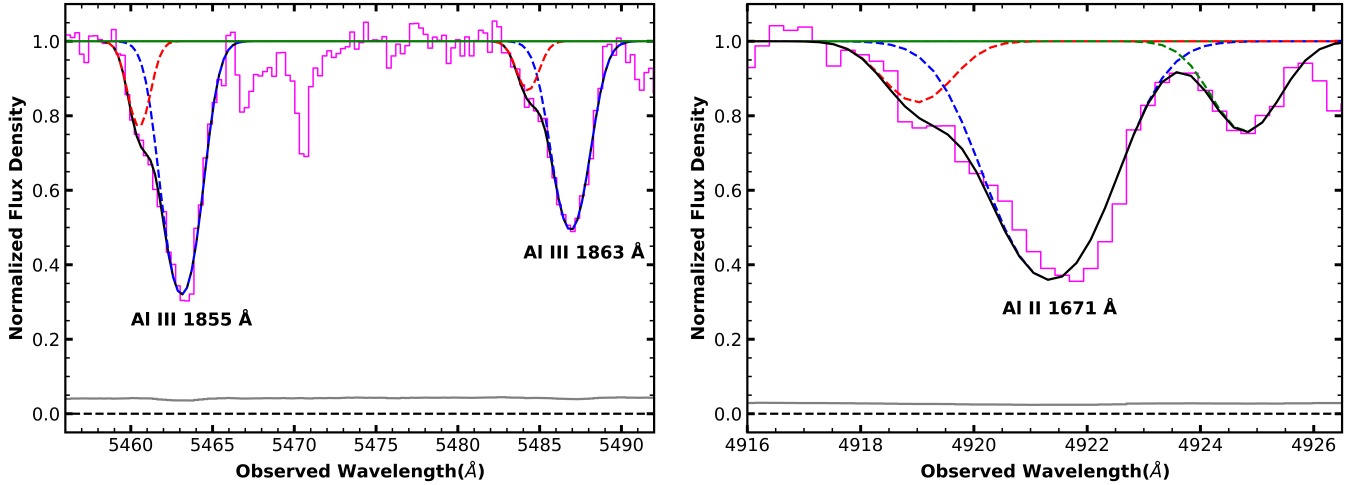


Figure 10. Multiple component Gaussian modeling for the Al transitions. The main outflow component is shown in blue with the secondary component shown in red and green (for Al II). The black curve shows the combined model for the troughs. The solid green lines represents the local continuum model. The gray line shows the noise in the VLT/X-shooter flux.

A.1.2. Si II

The absorption trough for the Si II* 1309 Å transition is well modeled by a single Gaussian component as shown in Fig. 3. However the Si II 1304 Å trough shows evidence for multiple components (four in particular, as can be noted by the two inflection points on the blue wing, and one more on the red wing). Therefore, we model the Si II trough with four Gaussian components, of which one has fixed centroid and width based on the Si II* 1309 profile. The other three components are allowed to have centroids and widths that vary independently, and the depths of all the four components are allowed to vary as well. The results for the best-fit model templates (determined by non-linear least squares) for these troughs are shown in Fig. 11.

A.2. Change in Column Density

We now investigate the effect of the different models on the column density measurement for our main outflow component. To do so, we obtain the column density of the main component (shown in blue in Figs. 10 and 11) from the multi component modeling and compare them with the column density obtained from the single Gaussian fitting shown in Figs. 2 and 3. We report

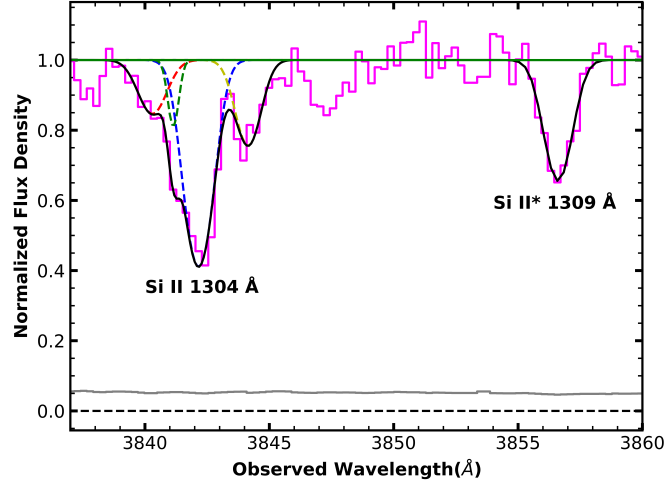


Figure 11. Multiple component Gaussian modeling for the Si II transitions. The main outflow component is shown in blue with the secondary components shown in red, green and yellow. The black curve shows the combined model for the troughs. The solid green lines represents the local continuum model. The gray line shows the noise in the VLT/X-shooter flux.

Table 4. Difference in Column Density Measurements based on the two approaches

Ion	ΔN_{ion} (%)
Al II	-4.5
Al III	-4.5
Si II	-2.7

the % change in the column density measurement due to the multiple component approach in Table 4. The difference for all three ions are less than 5% and therefore we use the one component Gaussian model for our analysis as it has fewer free parameters. We include this uncertainty due to our choice of models in the column densities reported in Table 2.